

Third-Harmonic and Intermodulation Distortion in Bulk Acoustic-Wave Resonators

David Garcia-Pastor¹, *Student Member, IEEE*, Carlos Collado¹, *Senior Member, IEEE*,
Jordi Mateu¹, *Senior Member, IEEE*, and Robert Aigner

Abstract—This article discusses on the measured third-order intermodulation (IMD3) products and third harmonics (H3) appearing in a set of six different solidly mounted resonators (SMR) and bulk acoustic-wave (BAW) resonators with different shapes and stack configurations. The discussion is supported by a comprehensive nonlinear distributed circuit model that considers the nonlinear effects potentially occurring in any layer of the resonator stack. The aluminum-nitride (AlN) and silicon-dioxide (SiO₂) layers are identified as the most significant contributors to the IMD3 and H3. The frequency profile of the third-order spurious signals also reveals that, in temperature-compensated resonators, where the SiO₂ layers are usually thicker, the remixing effects from the second-order nonlinear terms are the major contributors to the IMD3 and H3. These second-order terms are those that explain the second-harmonic (H2) generation, whose measurements are also reported in this article. Unique values of the nonlinear material constants can explain all the measurements despite the resonators have different shapes, resonance frequencies, and stack configurations.

Index Terms—Aluminum nitride (AlN), bulk acoustic wave (BAW), electroacoustic, nonlinear, nonlinearities, silicon dioxide SiO₂, solidly mounted resonators (SMRs), third-harmonic (H3), third-order intermodulation (IMD3), third-order intermodulation (IMD3) product.

I. INTRODUCTION

WITH the fast expansion of the current predominant technologies (LTE-A, IEEE wireless LAN standards, low-power wide-area networks, and so on) and the new incoming standards (5G-NR, IEEE 802.11ax), the mobile communication requirements are more stringent than ever. In this scenario, acoustic-wave technology has been playing a crucial role on the development of the RF filtering stages of the current portable devices [1], allowing the inclusion of more than 40 filters per device. Among acoustic technologies, bulk acoustic-wave (BAW) configuration provides many of the filters operating around 2 GHz and above [2].

Manuscript received May 3, 2019; revised November 15, 2019; accepted November 17, 2019. This work was supported in part by the Spanish Government under Grant TEC2017-84817-C2-2-R, Grant TEC2017-88343-C4-2-R, and Grant 2017 SGR 813, in part by the Universities and Research Secretary of the Generalitat de Catalunya, and in part by the European Social Fund under Grant 2018FL_B_00448. (*Corresponding author: David Garcia-Pastor.*)

D. Garcia-Pastor, C. Collado, and J. Mateu are with the Signal Theory and Communications Department, Universitat Politècnica de Catalunya, 08034 Barcelona, Spain (e-mail: david.garcia@tsc.upc.edu).

R. Aigner is with Qorvo, Inc., Orlando, FL 32703 USA.

Color versions of one or more of the figures in this article are available online at <http://ieeexplore.ieee.org>.

Digital Object Identifier 10.1109/TMTT.2019.2955135

Without detrimental to offering exceptional frequency-selective responses, acoustic filters exhibit an inherent nonlinear response due to the nature of the piezoelectric material and all other additional layers are used to create the electrodes and the acoustic reflector in the solidly mounted resonator (SMR) configuration. Such a nonlinear response might limit the application of these filters in the current and forthcoming spectrum scenarios.

In order to give response to this major concern, accurate modeling of the nonlinear response is an essential step toward the prediction and understanding of these undesired effects. Past studies proposed different nonlinear distributed models for acoustic devices [3]–[9]. Although those approaches used different circuit models, all of them made the assumption that the unique contributor to the nonlinear response was the piezoelectric layer (AlN). However, recent studies pointed out that other layers forming the resonator can also contribute to the nonlinear response. In particular, references [10] and [11] showed that the SiO₂ layers of the acoustic reflector may play a significant role on the generation of second harmonics (H2), what becomes especially relevant in temperature-compensated resonators, where SiO₂ layers are thicker than that in the nontemperature-compensated resonators. Collado *et al.* [11] also reports on H3 and IMD3 measurements for a single resonator, and clearly concludes that several nonlinear sources might exist to explain their behavior. Full understanding of the origin of the nonlinear effects indeed requires the identification of all the sources contributing to the overall nonlinear manifestations.

To this aim, this article focuses on the third-order nonlinear manifestations, by performing a detailed characterization of H3 and IMD3 occurring in six different resonators. All the resonators evaluated in this article have the same stack configuration, but with different layer thicknesses and shapes. The characterization process allows to identify the direct contribution and the remixing effects into the overall IMD3 and H3, and it provides a unique set of second- and third-order nonlinear constants of the AlN and SiO₂ that can explain all the measurements. Note that the fact of applying a unique model to emulate the behavior of several nonlinear manifestations and for different resonators supports the consistency and uniqueness of the solution.

The core of the article is organized as follows. Section II recalls the nonlinear constitutive equations and their implementation into the nonlinear distributed circuit model used in this article. Section III details on the characterized resonators

84 and outlines on their broadband linear frequency response
 85 as a previous step for the nonlinear characterization process.
 86 Section IV describes the measurements of the H2 and
 87 third-order spurious signals, H3 and IMD3, and it discusses
 88 about the potential contributing materials to the generation of
 89 these spurious signals.

90 II. NONLINEAR MODELS

91 As mentioned above, we make use of a distributed circuit
 92 model to emulate the nonlinear response of the measured
 93 SMR-BAW resonators. This model is based on the nonlin-
 94 ear Mason equivalent circuit of the piezoelectric layer [5]
 95 and includes the nonlinear equivalent circuits of the other
 96 layers [10], [11]. It basically consists on discretizing into
 97 elemental cells each potential contributing layer to the gener-
 98 ation of harmonics or IMD products. Then, all the elemental
 99 cells are cascaded together to model the whole resonator.
 100 The distributed model allows capturing the field distribution
 101 along each layer of interest and the inclusion of the nonlinear
 102 sources distributed along the stack of materials. This model
 103 was extensively reported in [9] and partially recalled below
 104 for the sake of a self-contained article.

105 Proper modeling of each elemental cell requires the formu-
 106 lation of the nonlinear constitutive equations at each mate-
 107 rial. For the piezoelectric case, those equations model the
 108 relation between the different field magnitude stress, strain,
 109 electric field, and electric displacement as T , S , E , and D ,
 110 respectively [5]. Those field magnitudes are related to each
 111 other by the use of different constants, being these c^E , e ,
 112 and ε^S as stiffness, piezoelectric, and dielectric constant,
 113 respectively. As detailed in [9], S and D field magnitudes are
 114 implemented in the nonlinear model as independent variables,
 115 giving the equations

$$116 \quad T = c^D S - \frac{e}{\varepsilon^S} D + T_c \quad (1)$$

$$117 \quad E = \frac{D - eS}{\varepsilon^S} - V_c. \quad (2)$$

118 The nonlinear sources T_c and V_c are

$$119 \quad T_c = \Delta T + \frac{e}{\varepsilon^S} \Delta D \quad (3)$$

$$120 \quad V_c = \frac{\Delta D}{\varepsilon^S} \Delta z \quad (4)$$

121 where $c^D = c^E + e^2/\varepsilon^S$ is the stiffened elasticity and Δz
 122 is the thickness of an elemental cell. ΔT and ΔD are the
 123 terms defining the nonlinear behavior of the piezoelectric layer,
 124 truncated to a third-order polynomial, as follows:

$$125 \quad \Delta T = c_2^E \frac{S^2}{2} - \varphi_3 \frac{E^2}{2} + \varphi_5 S E + c_3^E \frac{S^3}{6} + X_7 \frac{S E^2}{2} - X_9 \frac{S^2 E}{2} \quad (5)$$

$$126 \quad \Delta D = \varepsilon_2^S \frac{E^2}{2} - \varphi_5 \frac{S^2}{2} + \varphi_3 S E + \varepsilon_3^S \frac{E^3}{6} + X_9 \frac{S^3}{6} - X_7 \frac{S^2 E}{2}. \quad (6)$$

127 Those nonlinear terms are mathematically defined by differ-
 128 ent second-order (c_2^E , φ_3 , φ_5 , ε_2^S) and third-order coefficients
 129 (c_3^E , ε_3^S , X_7 , X_9) [9].

130 Fig. 1 depicts the equivalent circuit model of an elemental
 131 cell corresponding to the equations above, where the nonlinear
 132 sources T_c and V_c are included in the conventional distributed

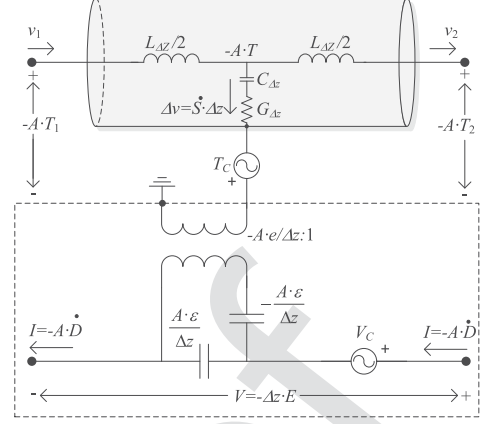


Fig. 1. Nonlinear unit cell of the piezoelectric layer [9].

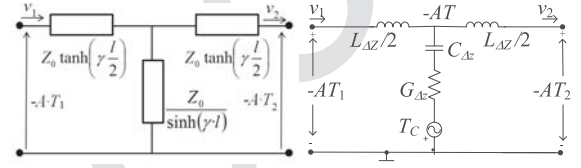


Fig. 2. Circuit models of the nonpiezoelectric layers. T-network equivalent circuit of an acoustic transmission line (left) and nonlinear unit cell of a discretized transmission line [11].

133 Mason model [6], [9]. The number of unit cells used depends
 134 on the smallest wavelength to analyze.

135 For the nonpiezoelectric layers, the model to be used
 136 depends on the potential nonlinear contribution of a given
 137 material [11]. In the case of assuming a linear layer, there is
 138 no need of discretizing the layer and a T-network equivalent
 139 circuit of an acoustic transmission line can be used, as shown
 140 in Fig. 2(left). However, when the nonlinearities of the layer
 141 need to be considered, the layer is discretized as per the
 142 elemental cell shown in Fig. 2(right). In this later case,
 143 the relation of the field magnitudes T and S , obeys

$$144 \quad T = c_{np} S + T_c \quad (7)$$

145 where T_c is the nonlinear source and can be read as

$$146 \quad T_c = \frac{1}{2} c_{2,np} S^2 + \frac{1}{6} c_{3,np} S^3. \quad (8)$$

147 The nonlinear terms in T_c are defined by a second-order
 148 ($c_{2,np}$) and a third-order ($c_{3,np}$) coefficient, where the subscript
 149 np indicates a given material ($np = \text{SiO}_2, \text{W}, \text{AlCu}, \text{SiN}$).

150 III. DEVICES AND LINEAR RESPONSE

151 This section outlines the six resonators tested in this article
 152 and their broadband measured input impedance along with the
 153 simulated impedance using the equivalent distributed model
 154 of Section II.

155 A. Description of the Resonators

156 Although being six different SMR BAW resonators, all of
 157 them present equal material distribution along the stack with
 158 different thicknesses accommodated to provide a proper linear
 159

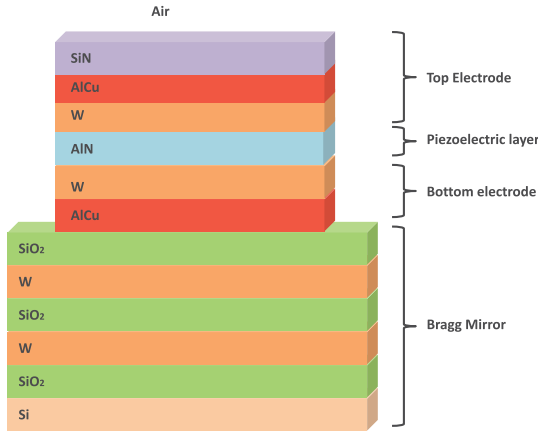


Fig. 3. Stack configuration of the measured SMR BAW devices.

TABLE I
BAW RESONATOR CHARACTERISTICS

Resonators	Mode	Band	Series	Shunt
R1	LTE-FDD	30	✓	
R2	LTE-FDD	30		✓
R3	Wi-Fi	2.4 GHZ	✓	
R4	Wi-Fi	2.4 GHZ		✓
R5	LTE-FDD	B7	✓	
R6	LTE-FDD	B7		✓

159 response. The layer distribution of the resonator is outlined
 160 in Fig. 3. The six resonators can be classified into three
 161 groups. Each group consists of two resonators, which would
 162 correspond to a series and a shunt resonator of a ladder con-
 163 figuration filter. Each group of resonators has been designed to
 164 operate at different frequency ranges, which correspond to dif-
 165 ferent communication services. The resonators differ on their
 166 areas, shapes, and layer thicknesses. Although the knowledge
 167 of the exact dimension of the resonators is mandatory for a
 168 proper modeling of the devices, those cannot be disclosed here
 169 for confidential reasons. Table I identifies each resonator with
 170 different names for the sake of clarity.

171 It is worth mentioning that R1 and R2 significantly differ
 172 from the other four resonators in the thickness of the SiO₂
 173 layers, which is set considerably thicker in order to provide
 174 a compensated temperature response.

175 **B. Linear Simulations**

176 An unavoidable initial step for a unified nonlinear modeling
 177 is to accurately emulate the linear broadband response of the
 178 resonator. The matching of the measured and simulated input
 179 impedances by means of a distributed model is crucial to
 180 emulate the field distributions at any point along the stack
 181 at the fundamental frequencies, f_1 and f_2 , and therefore the
 182 distribution of the nonlinear sources along the stack according
 183 to (3)–(8). These nonlinear sources create spurious signals at
 184 given mixed frequencies (for example, $2f_1$, $3f_1$, and $2f_1 - f_2$),
 185 whose output powers depend on how their field distributions
 186 couple to the load [12].

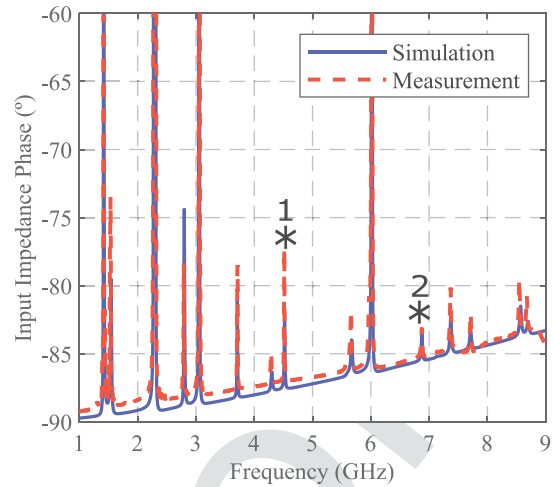


Fig. 4. Simulated and measured broadband phase frequency response of R2. Spurious resonances affecting the nonlinear response are marked with asterisks 1 and 2.

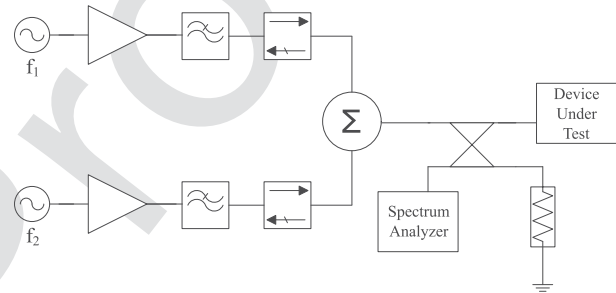


Fig. 5. H2, IMD3, and H3 measurement system.

187 As an example, Fig. 4 illustrates the agreement between the
 188 measured and modeled responses for resonator R2. Fine trim-
 189 ming within the manufacturing tolerances of layer thicknesses
 190 from the given nominal values has been performed in order
 191 to provide an accurate fitting through the whole measured
 192 frequency range. The broadband (from 1 to 9 GHz) input
 193 impedance phase demonstrates the accuracy of the modeling
 194 on following all the resonances appearing along the whole
 195 frequency range. Asterisks 1 and 2 in Fig. 4 indicate the
 196 resonances that have an impact on the H2 and H3 frequency
 197 responses, as it will be discussed in Section IV.

198 The linear response of R1 along with the characterization
 199 of H2 was reported in [11].

200 **IV. NONLINEAR MEASUREMENTS**

201 This section provides an extensive characterization of the
 202 nonlinear response of the resonators of Table I by performing
 203 the measurements of H2, H3, and IMD3, using the measure-
 204 ment setup outlined in Fig. 5. The experiment consists of
 205 driving the resonators with two fundamental high-power tones
 206 (at f_1 and f_2) and measuring, using a broadband low-PIM
 207 90° hybrid coupler, the generated power reflected by the
 208 resonators. The floor level of the H2, H3, and IMD3 of
 209 the measurement system was obtained with the probe lifted
 210 in air, resulting in -80 , -90 , and -90 dBm, respectively.

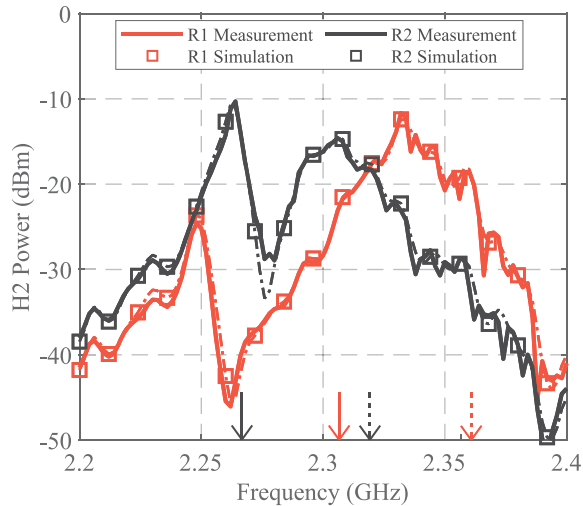


Fig. 6. $H_2(2 \cdot f_1)$ measurements and simulations for the B30 resonators. Continuous and dashed arrows indicate the series and shunt resonances, respectively.

211 The fundamental tones are both swept over 200-MHz range
 212 and, in order to avoid potential thermal effects on the gener-
 213 ation of IMD3, the two fundamental tones are set 10 MHz
 214 apart in frequency [9].

215 From the modeling point of view, the piezoelectric layer
 216 has been discretized into 60 elemental cells and the nonpiezo-
 217 electric layers into 100 elemental cells, which guarantees to
 218 follow the field magnitude distribution even at those frequen-
 219 cies where a sharp variation occurs. For simplicity, adhesion
 220 layers are not included in the simulations. Their effect on the
 221 nonlinear response was shown to be negligible. The nonlinear
 222 response of the whole circuit was obtained with harmonic
 223 balance simulations using Advanced Design System.

224 A. H_2 Measurements

225 Although this article focuses on the third-order nonlinear
 226 effects, measurements of the second harmonics have also been
 227 performed on the six resonators. The reason for this is twofold.
 228 First, this confirms the contribution of SiO_2 layers on the
 229 generation of H_2 , which was postulated in [11]. Note that this
 230 statement was obtained from the measurements of R1, and
 231 here is confirmed with the additional measurements of R2,
 232 the other temperature-compensated resonator. Second, and as
 233 mentioned in [11], the second-order coefficients, both the SiO_2
 234 layer and the piezoelectric layer AlN, could also contribute to
 235 the generation of the third-order nonlinear effects due to a
 236 remixing process, so those coefficients need to be considered
 237 as potential contributors to the H_3 and the IMD3.

238 Figs. 6–8 show how the second-order coefficients
 239 ($\varphi_5 = -18.7 \cdot e$, $\varepsilon_2 = 20 \cdot \varepsilon^S \cdot e/c^E$, and $c_{2,\text{SiO}_2} = -6.4 \cdot c_{\text{SiO}_2}$)
 240 published in [11] explain with good agreement the H_2 mea-
 241 surements of all the resonators. The x -axis indicates the central
 242 frequency between the fundamental signals. As it is well
 243 known, the maximum H_2 that appears between the series
 244 and shunt resonances (marked with arrows in the figures) is
 245 dominated by the term φ_5 for all the resonators, whereas the

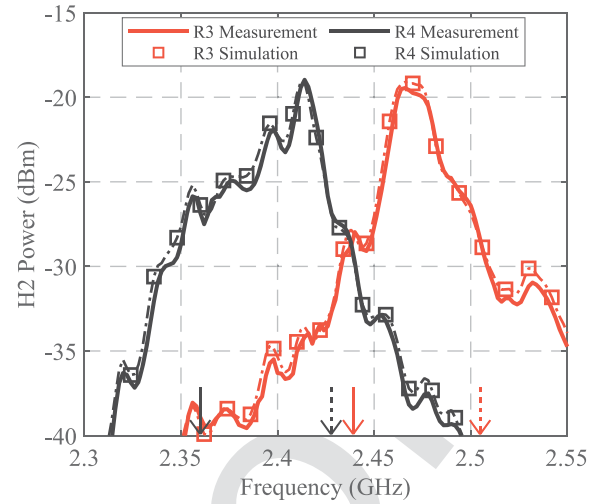


Fig. 7. $H_2(2 \cdot f_1)$ measurements and simulations for the Wi-Fi resonators. Continuous and dashed arrows indicate the series and shunt resonances, respectively.

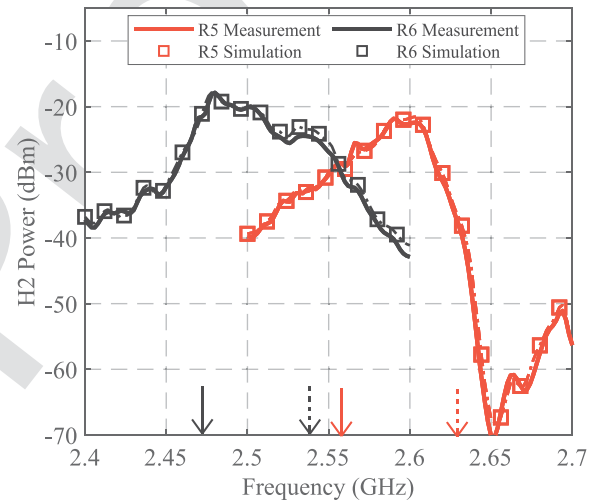


Fig. 8. $H_2(2 \cdot f_1)$ measurements and simulations for the B7 resonators. Continuous and dashed arrows indicate the series and shunt resonances, respectively.

246 term ε_2 affects to the out of band H_2 . The resonators R1 and
 247 R2 show an anomalous high H_2 peak at 2.25 and 2.26 GHz,
 248 respectively, just below their series resonances (2.31 and
 249 2.33 GHz). Those peaks are dominated by the second-order
 250 term c_{2,SiO_2} of the elastic constant of the SiO_2 layers, which
 251 was set to $c_{2,\text{SiO}_2} = -6.4 \cdot c_{\text{SiO}_2}$ [11]. This phenomena
 252 were already reported in [11] for the R1 resonator and it
 253 appears again for the R2 resonator. At twice the high peak
 254 frequency (4.50 and 4.52 GHz), the generated H_2 is enhanced
 255 by a high-order resonance, which can be identified with the
 256 asterisk number 1, in the input impedance of Fig. 4. Note that
 257 this also demonstrates the usefulness of using a distributed
 258 model and the importance of having a good matching between
 259 the simulations and measurements of the broadband linear
 260 response.

261 For R3–R6, the H_2 response is dominated by the
 262 second-order terms coming from the AlN layer. The
 263 second-order elastic constant of the SiO_2 layers only
 264 contributes to around 1 dB to the maximum H_2 output power.

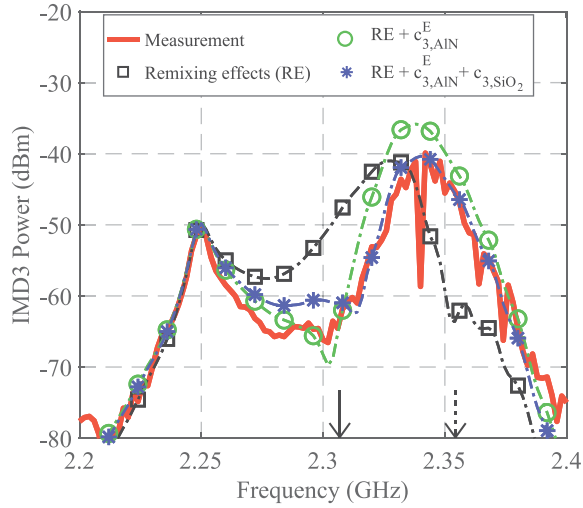


Fig. 9. IMD3 ($2 \cdot f_1 - f_2$) measurement and simulations for resonator R1. Continuous and dashed arrows indicate the series and shunt resonances, respectively.

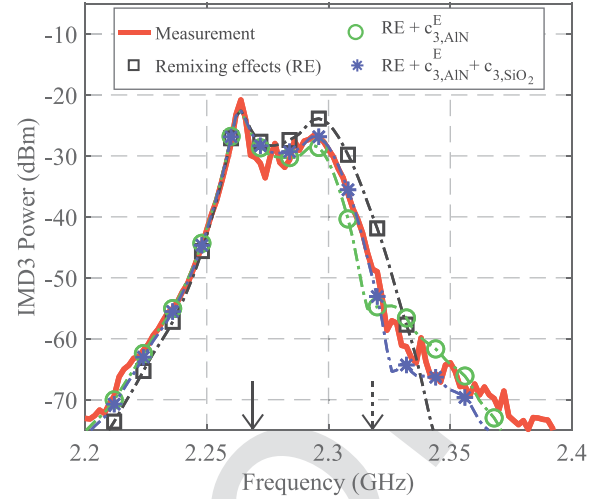


Fig. 10. IMD3 ($2 \cdot f_1 - f_2$) measurement and simulations for resonator R2. Continuous and dashed arrows indicate the series and shunt resonances, respectively.

265 For an accurate agreement between the measurements and the
 266 simulations, the broadband measurement system effects
 267 have been included in all the simulations. The most com-
 268 mon effect of the nonideal measurement system is the
 269 ripple depicted in all the measurements and the reduction in
 270 the H2 output power at higher frequencies due to the limited
 271 bandwidth of the components used in the measurement system,
 272 which is especially relevant for the R5 resonator at frequen-
 273 cies higher than 2.6 GHz.

274 B. IMD3 Measurements

275 1) *IMD3 Due to Remixing Effects:* The next step of the
 276 characterization consists on analyzing the IMD3 of all the
 277 resonators and discerns the contribution of the second-order
 278 nonlinear terms due to the remixing phenomena.

279 Fig. 9 shows the measured IMD3 of the resonator R1 in
 280 thick red line. The x -axis corresponds to the central frequency
 281 of the two fundamental tones, i.e., $f_0 = (f_1 + f_2)/2$, which is
 282 swept from 2.2 to 2.4 GHz. These measurements correspond
 283 to the spurious signal at $2f_1 - f_2$, when the input power level
 284 of the two fundamental tones is set to 20 dBm and the space
 285 frequency between the two tones ($\Delta f = f_2 - f_1$) is kept to
 286 10 MHz along the whole experiment. Fig. 9 also shows, in
 287 squared dashed black line, the contribution to the IMD3 from
 288 the second-order nonlinear terms corresponding to AlN and
 289 SiO₂ due to remixing effects. Similar measurements were
 290 reported in [11], and we concluded that the remixing effects
 291 could not solely explain the measured IMD3, because in some
 292 frequency ranges, the simulated IMD3 is higher than the
 293 measured value and in others lower. For the R2 resonator,
 294 as is depicted in Fig. 10, something similar happens and
 295 the simulated response overestimates the measurements at
 296 frequencies near the shunt resonance. Those experiments
 297 indicate that other nonlinear sources must exist beyond the
 298 remixing effects. It is remarkable that the IMD3 for these R1
 299 and R2 exhibits an additional peak at 2.25 and 2.26 GHz,
 300 respectively, below their series resonances. These peaks appear

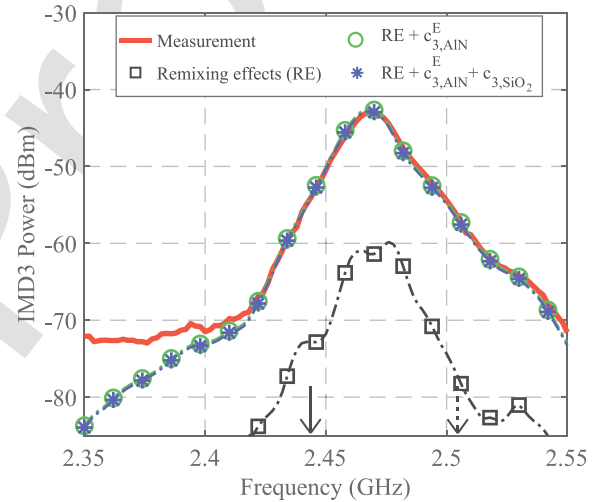


Fig. 11. IMD3 ($2 \cdot f_1 - f_2$) measurement and simulations for resonator R3. Continuous and dashed arrows indicate the series and shunt resonances, respectively.

301 at the same frequencies compared with those appearing in their
 302 corresponding H2 (see Fig. 6). It is clear then that those peaks
 303 are generated by the second-order remixing effects mainly due
 304 to the SiO₂ layers.

305 2) *IMD3 Due to AlN Third-Order Elastic Constant:* To
 306 identify the third-order nonlinear terms of the different layers
 307 that additionally could contribute to the IMD3, we start by
 308 assuming that only one layer contributes to the direct genera-
 309 tion at a time. This is setting all the third-order nonlinear
 310 constants to zero but one. We tested the potential values of
 311 $c_{3,AiN}^E$, $c_{3,W}$, $c_{3,AiCu}$, and so on, and note that for all these
 312 cases, it is always considered the contribution of the remixing
 313 effect coming from the second-order terms of AlN and SiO₂
 314 found in Section V. None of them adjusted all the measure-
 315 ments but the term $c_{3,AiN}^E = -110 \cdot c^D$ of the AlN layer.
 316 This value has been previously reported in [6] and [9] and fits
 317 perfectly the IMD3 measured of the resonators R3–R6, as it
 318 can be seen in dashed lines with green circles in Figs. 11–14.

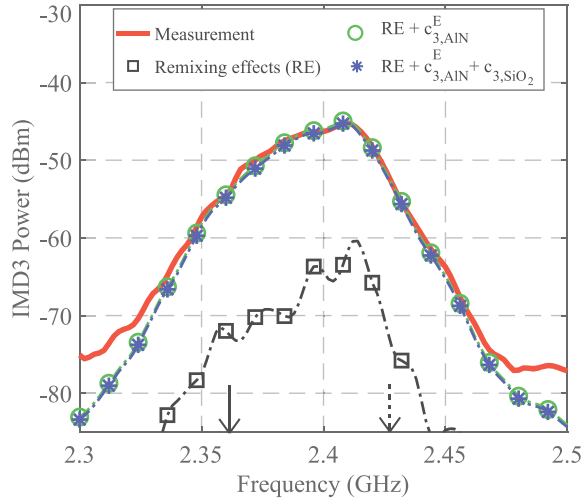


Fig. 12. IMD3 ($2 \cdot f_1 - f_2$) measurement and simulations for resonator R4. Continuous and dashed arrows indicate the series and shunt resonances, respectively.

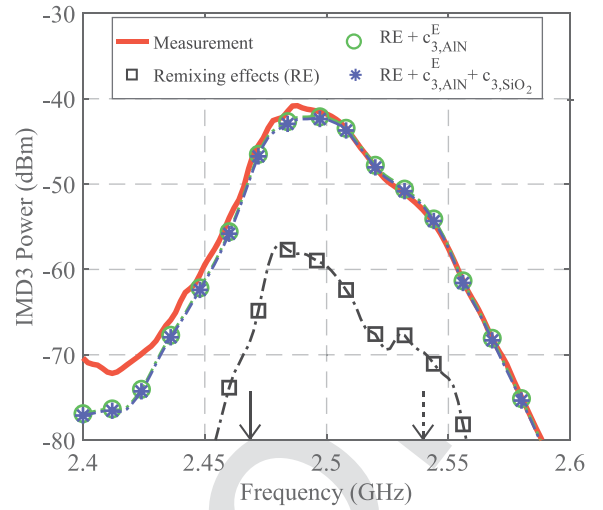


Fig. 14. IMD3 ($2 \cdot f_1 - f_2$) measurement and simulations for resonator R6. Continuous and dashed arrows indicate the series and shunt resonances, respectively.

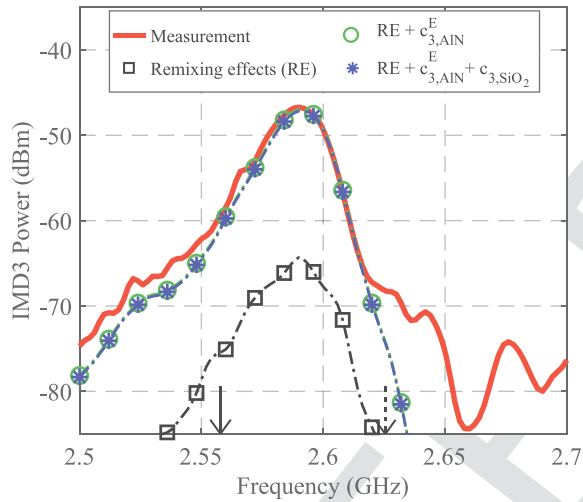


Fig. 13. IMD3 ($2 \cdot f_1 - f_2$) measurement and simulations for resonator R5. Continuous and dashed arrows indicate the series and shunt resonances, respectively.

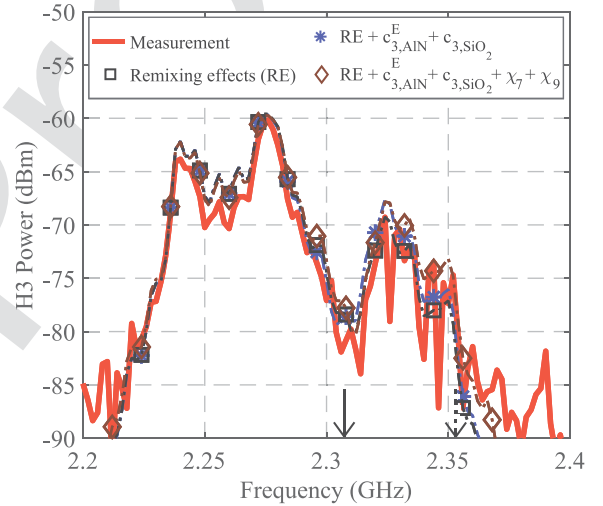


Fig. 15. H3 ($3 \cdot f_1$) measurement and simulations for the test resonator R1. Continuous and dashed arrows indicate the series and shunt resonances, respectively.

319 The simulated IMD3 of the R2 resonator (see Fig. 10)
 320 also presents a better fitting with the measurements when this
 321 term is included, lowering the IMD3 that the remixing effects
 322 overestimate. For the first resonator R1, the adjustment of the
 323 IMD3 significantly improves (see Fig. 9), but still, the IMD3 is
 324 overestimated by 5 dB around the resonance frequency.

325 To capture all the nonlinear contributors fully, we look
 326 for an additional direct contribution that could affect mainly
 327 the R1 resonator and remain unchanging the IMD3 of the other
 328 resonators.

329 3) *IMD3 Due to SiO₂ Third-Order Elastic Constant*: As
 330 it has been mentioned before, R1 and R2 has thicker layers
 331 of SiO₂ in comparison with the other resonators. Therefore,
 332 its third-order elastic constant is the best potential candi-
 333 date. Adding a value of $c_{3,\text{SiO}_2} = 30 \cdot c_{\text{SiO}_2}$, the simulated
 334 IMD3 adjusts the experimental data as it can be seen in dashed
 335 lines with blue asterisks in Figs. 9 and 10.

336 Once identified this third-order nonlinear term, the other
 337 four resonators have been analyzed using the set of constants
 338 (φ_5 , ε_2^S , c_{2,SiO_2}^E , c_3^E , and c_{3,SiO_2}^E). Figs. 11–14 show that this
 339 additional term does have no impact at all into the IMD3 of
 340 those resonators.

C. H3 Measurements

341 The H3 generation must be consistent with the set of
 342 nonlinear parameters described in the previous sections.

343 Figs. 15 and 16 compare the measured H3 (R1 and R2) with
 344 the simulated H3 due to remixing effects (black squares) and the
 345 set of five parameters described previously (blue asterisks),
 346 where the x -axis represents the fundamental frequency.
 347 It is clear that the H3 in the temperature-compensated res-
 348 onators R1 and R2 is dominated by remixing effects. The
 349 lower frequency peaks appearing in Figs. 15 and 16 at 2.24 and
 350

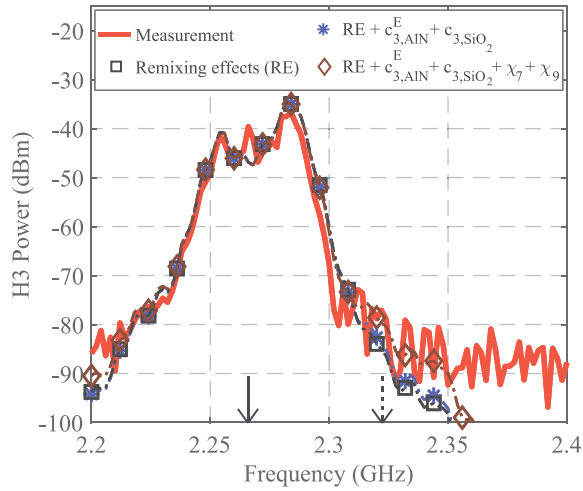


Fig. 16. H3 ($3 \cdot f_1$) measurement and simulations for the test resonator R2. Continuous and dashed arrows indicate the series and shunt resonances, respectively.

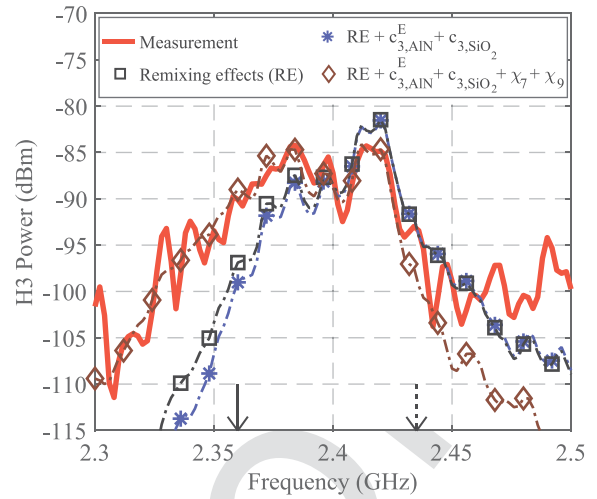


Fig. 18. H3 ($3 \cdot f_1$) measurement and simulations for the test resonator R4. Continuous and dashed arrows indicate the series and shunt resonances, respectively.

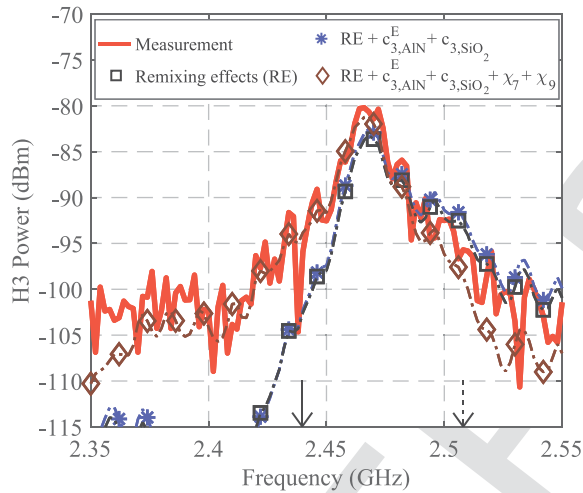


Fig. 17. H3 ($3 \cdot f_1$) measurement and simulations for the test resonator R3. Continuous and dashed arrows indicate the series and shunt resonances, respectively.

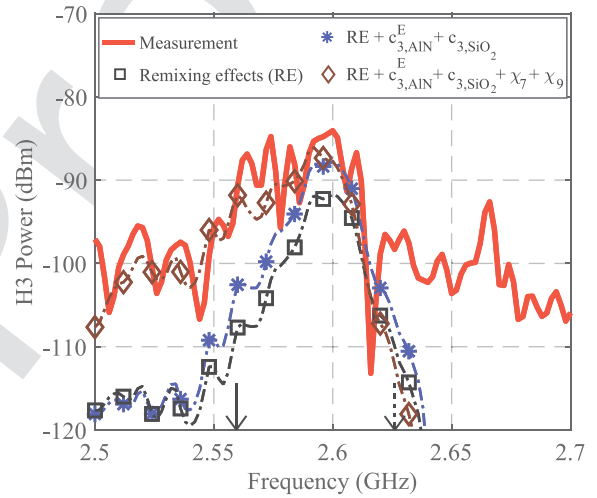


Fig. 19. H3 ($3 \cdot f_1$) measurement and simulations for the test resonator R5. Continuous and dashed arrows indicate the series and shunt resonances, respectively.

2.26 GHz, respectively, have the same origin that the peaks appear at their counterparts H2 and IMD3. The highest peaks that appear at 2.27 and 2.28 GHz for R1 and R2, respectively, are due to high-order resonances at 6.81 and 6.84 GHz (depicted with the asterisk number 2 in Fig. 4) and note that the H3 does not show a conventional frequency pattern with the highest values around the resonance frequency, whereas a small hill appears around the resonance of R1 and the H3 of R2 does not show remarkable values around its resonance frequency.

The measured H3 of the noncompensated resonators R3–R6 (see Figs. 17–20) shows a more conventional frequency pattern with maximum values around their resonance frequencies. The simulated H3 of these resonators have the same order of magnitude than the measurements when the third-order terms $c_{3,AlN}^E$ and $c_{3,SiO2}$ are considered (blue asterisks).

A better adjustment of the H3 of these four resonators can be achieved with the inclusion of additional third-order nonlinear

constants $X_9 = 67 \cdot e$ and $X_7 = -4 \cdot 10^{-9}$ for the AlN layer [see (5), (6)]. The term X_9 is the extension up to a third order of the term φ_5 , which dominates the H2 generation around the resonance frequency, and it controls the maximum level of the H3, because X_9 multiplies S^3 in ΔD [see (6)]. The term X_7 balances the frequency pattern at both edges of the resonance frequency, since it always multiplies the electric field in ΔD and ΔT in (5) and (6).

Those two new terms X_9 and X_7 do not have an effect on the H3 of the R1 and R2 resonators (see brown diamonds in Figs. 15 and 16), since their H3 is dominated by remixing effects.

Finally, it is important to outline that the IMD3 of all the resonators is not affected by these new two third-order terms. Simulations of IMD3 considering all the terms in Table II are not included in Figs. 9–14 for the sake of clarity of the pictures, since the simulated traces would overlap the blue asterisk traces.

369
370 AQ:4
371
372
373
374
375
376
377
378
379
380
381
382
383
384
385
386

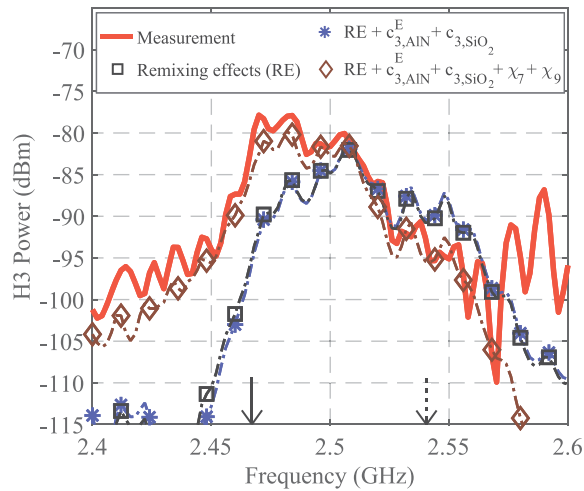


Fig. 20. H3 ($3 \cdot f_1$) measurement and simulations for the test resonator R6. Continuous and dashed arrows indicate the series and shunt resonances, respectively.

TABLE II
NONLINEAR COEFFICIENTS

Nonlinear coefficient	Value
φ_5	$-18.7 \cdot e$
ε_2	$20 \cdot \varepsilon^S \cdot e/c^E$
c_{2,SiO_2}	$-6.4 \cdot c_{SiO_2}$
$c_{3,AlN}^E$	$-110 \cdot c^D$
c_{3,SiO_2}	$30 \cdot c_{SiO_2}$
X_9	$67 \cdot e$
X_7	$-4 \cdot 10^{-9}$

Table II summarizes all seven nonlinear coefficients contributing to H2, H3, and IMD3 responses and their value.

V. CONCLUSION

This article outlines the major contributors into the nonlinear spurious manifestations at H2, H3, and IMD3, by providing a systematic characterization process and an accurate modeling of the acoustic resonators.

The modeling consisted of a distributed Mason model that has been used to successfully evaluate the second- and third-order spurious signals occurring in acoustic resonators. This provides, therefore, a unified description of the nonlinear behavior of such devices. This model has demonstrated to be valid for six different resonators evaluated in this article, which gives confidence on the uniqueness and consistency of the solution provided. The characterization process consists of a systematic procedure that allows identifying the different

sources contributing to the nonlinear manifestation by sequentially adding different nonlinear contributors. This starts by the second-order nonlinear terms that explain the H2 values. Note that those terms also contribute to the H3 and IMD3 manifestations through a remixing phenomenon. In particular, the role of the SiO₂ layers through the term c_{2,SiO_2} is crucial for the generation of IMD3 and H3 in the temperature-compensated resonators.

For the noncompensated resonators, our experiments confirm that the IMD3 around resonance is dominated by the term $c_{3,AlN}^E$. However, the H3 is dominated by the remixing effects due to φ_5 and c_{2,SiO_2} , and two additional third-order terms (X_7 and X_9) have been included for a better adjustment of the H3 of all the resonators. These two additional terms do not affect to the IMD3 but additional measurements (other resonators and/or other experiments) should be performed to guarantee the uniqueness and consistence of the solution including these terms.

REFERENCES

- [1] R. Ruby, "A snapshot in time: The future in filters for cell phones," *IEEE Microw. Mag.*, vol. 16, no. 7, pp. 46–59, Aug. 2015.
- [2] R. Aigner, "Filter technologies for converged RF-frontend architectures: SAW, BAW and beyond," in *Proc. Top. Meeting Silicon Monolithic Integr. Circuits RF Syst. (SiRF)*, New Orleans, LA, USA, 2010, pp. 136–139.
- [3] C. Collado, E. Rocas, J. Mateu, A. Padilla, and J. M. O'Callaghan, "Nonlinear distributed model for bulk acoustic wave resonators," *IEEE Trans. Microw. Theory Techn.*, vol. 57, no. 12, pp. 3019–3029, Dec. 2009.
- [4] D. A. Feld, D. S. Shim, S. Fouladi, and F. Bayatpur, "Advances in nonlinear measurement & modeling of bulk acoustic wave resonators (invited)," in *Proc. IEEE Int. Ultrason. Symp.*, Chicago, IL, USA, Sep. 2014, pp. 264–272.
- [5] D. S. Shim and D. A. Feld, "A general nonlinear mason model of arbitrary nonlinearities in a piezoelectric film," in *Proc. IEEE Int. Ultrason. Symp.*, San Diego, CA, USA, Oct. 2010, pp. 295–300.
- [6] D. S. Shim and D. A. Feld, "A general nonlinear Mason model and its application to piezoelectric resonators," *Int. J. RF Microw. Comput.-Aided Eng.*, vol. 21, no. 5, pp. 486–495, Sep. 2011.
- [7] Y. Cho and J. Wakita, "Nonlinear equivalent circuits of acoustic devices," in *Proc. IEEE Int. Ultrason. Symp.*, Baltimore, MD, USA, vol. 2, Oct./Nov. 1993, pp. 867–872.
- [8] D. A. Feld and D. S. Shim, "Determination of the nonlinear physical constants in a piezoelectric AlN film," in *Proc. IEEE Int. Ultrason. Symp.*, San Diego, CA, USA, Oct. 2010, pp. 277–282.
- [9] E. Rocas, C. Collado, J. Mateu, N. D. Orloff, J. C. Booth, and R. Aigner, "Electro-thermo-mechanical model for bulk acoustic wave resonators," *IEEE Trans. Ultrason., Ferroelectr., Freq. Control*, vol. 60, no. 11, pp. 2389–2403, Nov. 2013.
- [10] D. Garcia-Pastor *et al.*, "Nonlinear effects of electrode and Bragg reflector materials in BAW resonators," in *Proc. IEEE Int. Ultrason. Symp.*, Washington, DC, USA, Sep. 2017, pp. 1–4.
- [11] C. Collado *et al.*, "Nonlinear effects of SiO₂ layers in bulk acoustic wave resonators," *IEEE Trans. Microw. Theory Techn.*, vol. 66, no. 4, pp. 1773–1779, Apr. 2018.
- [12] J. Mateu, C. Collado, O. Menéndez, and J. M. O'Callaghan, "A general approach for the calculation of intermodulation distortion in cavities with superconducting endplates," *Appl. Phys. Lett.*, vol. 82, no. 1, pp. 97–99, Jan. 2003.